Magnetic structures of Mn-rich and of Fe-rich $TmMn_{6-x}Fe_xSn_6$ stannides with (Mn, Fe) kagome networks and related ^{119}Sn hyperfine magnetic fields

G. Venturini,[1,*] B. Malaman,[1,†] G. Le Caër,[2,‡] and T. Mazet[1,§]

[1]*Université de Lorraine, Centre national de la recherche scientifique (CNRS), Institut Jean Lamour (IJL), F-54000 Nancy, France*

[2]*Université de Rennes I, CNRS, Institut de Physique de Rennes (IPR)—UMR 6251, F-35000 Rennes, France*

(Received 15 July 2021; revised 4 November 2021; accepted 12 November 2021; published 30 November 2021)

Stannides $TmMn_{6-x}Fe_xSn_6$, with hexagonal $HfFe_6Ge_6$-type structures, were studied by x-ray and neutron diffraction, magnetic measurements, and by ^{119}Sn Mössbauer spectroscopy. Transition metal atoms form kagome networks in (001) planes with an intraplanar ferromagnetic coupling of their moments. At temperatures $>\sim$20 to 50 K, Mn-rich stannides ($x = 0.4, 0.6, 1.2$) have an AFII easy-plane antiferromagnetic (AFM) structure, with interplanar couplings $++--$ along the c axis. The thulium sublattice orders magnetically at low temperature. The complexity of the resultant neutron diffraction patterns arises from a mixture of several magnetic phases, some being incommensurate. The Tm sublattice does not order >1.6 K in Fe-rich stannides ($x = 4.25, 4.5, 5.0$). Fe-rich stannides have an AFI AFM structure, this time with interplanar couplings $+-+-$. The $M = Mn/Fe$ magnetic moments are directed along the c axis for $x = 5$ at any temperature. Further, neutron diffraction shows that moments rotate from the c axis toward the basal plane >4.2 K with maximum rotation angles of $\sim$70° and $\sim$55° reached at $\sim$50 and $\sim$80 K for $x = 4.25$ and 4.50, respectively. Transferred hyperfine fields at tin sites of $TmMn_{6-x}Fe_xSn_6$ stannides are the moduli of ^{119}Sn vectorial hyperfine magnetic fields that are modeled for the AFI and AFII magnetic structures, assuming a random substitution of Mn with Fe. Models involve sums of dipolar-type and of isotropic vector components with simple assumptions about the model parameters. The transferred hyperfine magnetic fields at ^{119}Sn nuclei are measured by Mössbauer spectroscopy. The hyperfine magnetic fields of Sn atoms, whose six transition metal nearest neighbors are ferromagnetically coupled, are predicted and observed to vary linearly with their number of Fe first nearest neighbors. The hyperfine magnetic fields on Sn atoms sandwiched between two AFM coupled kagome planes are expected proportional to $|p_2 - p_1|$, where one of the two kagome planes contains p_1 Fe first nearest neighbors and the other p_2. Tin atoms with a ferromagnetic first nearest neighbor shell experience negative hyperfine fields in Mn-rich stannides, whereas they experience positive hyperfine fields in the Fe-rich stannides. This change is explained by a change of sign of the isotropic hyperfine magnetic fields which occurs when going from Mn- to Fe-rich stannides.

DOI: 10.1103/PhysRevB.104.184433

I. INTRODUCTION

The hexagonal $HfFe_6Ge_6$-type structure of RM_6Sn_6 stannides, space group $P6/mmm$ (Fig. 1), is first characterized by three crystallographic sites, namely, 2c, 2d, and 2e, which are equally occupied by Sn atoms. Second, the crystallographic site 6i is occupied by M transition metal atoms, where M is Mn or Fe herein. Finally, the crystallographic site 1a is occupied by rare-earth atoms R (Fig. 1, Table S1 in the Supplemental Material [1]). Manganese atoms form kagome networks (Fig. S1 in the Supplemental Material [1]) in (001) planes (ab planes), also called kagome planes from now on.

Some recent studies (Refs. [2–12] and Sec. I in the Supplemental Material [1]), deal with transition-metal-based kagome magnets, a class of materials which is of fundamental importance. They include, among others, RM_6Sn_6 stannides. These studies focus on the physical consequences of the interplay between lattice geometry and electron correlation.

Most previous studies of RM_6Sn_6 stannides focused on crystallographic characteristics (Fig. 1) and on magnetic properties and structures. In addition, ^{119}Sn Mössbauer spectroscopy yielded detailed information on hyperfine magnetic fields in stannides, notably in RMn_6Sn_6 and RFe_6Sn_6 (R = Li, Mg, Sc, Pr-Sm, Gd-Lu, U) [13–26]. Here, ^{119}Sn hyperfine magnetic fields provide invaluable information on the local evolution of magnetic structure.

This paper is devoted to $TmMn_{6-x}Fe_xSn_6$ stannides, either Mn-rich ($x = 0.4, 0.6, 1.2$) or Fe-rich ($x = 4.25, 4.5, 5.0$). A $TmMn_{6-x}Fe_xSn_6$ stannide might form for any x, as $TmMn_6Sn_6$ and $TmFe_6Sn_6$ both crystallize with the $HfFe_6Ge_6$-type structure. Our aim was, first, to follow the effect of the substitution of Mn with Fe on magnetic structures, as studied by magnetic measurements and neutron diffraction and, second, its effect on transferred hyperfine magnetic fields at ^{119}Sn nuclei. Complex magnetic structures are observed at low temperatures in Mn-rich stannides because of the ordering of the Tm magnetic moments. By contrast, magnetic structures are simpler in Fe-rich stannides because the Tm magnetic moments do not order >1.6 K. Two simple "high-temperature" antiferromagnetic (AFM) structures, named AFII and AFI, are observed from neutron diffraction patterns. They are characterized by an ordering of the

*Deceased.
†bernard.malaman@univ-lorraine.fr
‡gerard.le-caer@univ-rennes1.fr
§thomas.mazet@univ-lorraine.fr

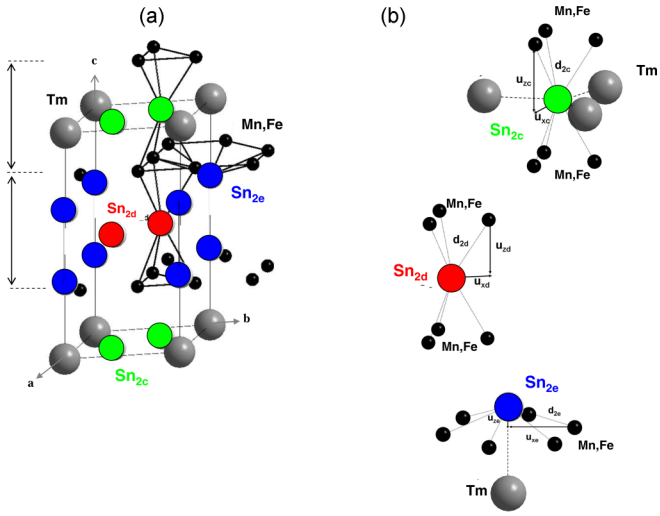

FIG. 1. (a) HfFe6Ge6-type structure of $Tm(Mn, Fe)_6Sn_6$. (b) Sn2c, Sn2d, and Sn2e tin sites with their first (Mn,Fe) and Tm neighbors.

transition metal moments which are ferromagnetically coupled in their (0 0 1) kagome planes [24]. These moments lie in the kagome planes in the Mn-rich stannides and are perpendicular to them, at least at 4.2 K, in the Fe-rich stannides (Fig. 2). Successive ferromagnetic (0 0 1) kagome planes are coupled along [0 0 1] according to sequences $++--$ and $+-+-$ for AFII and AFI, respectively [20,25] (Fig. 2).

Above 324 K, $TmMn_6Sn_6$ exhibits an easy-plane AFII AFM structure [25]. An easy-axis AFI-type structure is observed instead in $TmFe_6Sn_6$, at $T >\sim 1.6$ K, as in most $HfFe_6Ge_6$-type RFe_6Sn_6 stannides [25]. The Fe moments $\mu_{Fe} = 2.40(4)\mu_B$ at 2 K are directed along the c axis.

In practice, $TmFe_6Sn_6$ is slightly understoichiometric in Tm, with a composition $Tm_{1-\delta}Fe_6Sn_6$ ($\delta \approx 0.1$) [25]. X-ray diffraction patterns at room temperature (RT, nominally 295 K) indicate that Mn-rich $TmMn_{6-x}Fe_xSn_6$ stannides are essentially stoichiometric in Tm, while the Fe-rich ones, $Tm_{1-\delta}Mn_{6-x}Fe_xSn_6$, are slightly understoichiometric in Tm with $\delta \approx 0.05$ (Table S2 in the Supplemental Material [1]). The nominal composition $TmMn_{6-x}Fe_xSn_6$ will still be used hereafter.

The transferred magnetic hyperfine fields at ^{119}Sn nuclei are interpreted with a model whose physical basis finds a justification in first-principles electronic structure calculations [13,17]. It combines both dipolar and isotropic magnetic field components with the additional assumption of a random distribution of Mn and Fe on the 6i sites. The predicted hyperfine magnetic fields are then compared with hyperfine magnetic fields obtained from ^{119}Sn Mössbauer spectra. However, it is very difficult to confidently differentiate the effects of complex low-temperature magnetic structures on the ^{119}Sn Mössbauer spectra from those of the disordered substitution of Mn with Fe (Fig. 2 and Fig. S7 in the Supplemental Material [1]). To circumvent these difficulties, the magnetic structures AFI and AFII were given a major role to compare experimental and predicted hyperfine magnetic fields.

II. EXPERIMENTAL METHODS

A. Materials

The samples were prepared in an induction furnace starting from stoichiometric mixtures of elements: Tm from Alphaceasar, 99.9%; Fe from Cerac, 99.95%; Mn from Chempur, 99.99%; and Sn from Chempur, 99.99%. As-cast ingots were annealed at 1123 K for 1 week and quenched in water. Phases were identified by x-ray powder analysis (Xpert Pro diffractometer CuKα). Low-intensity peaks due to "impurities" were attributed, respectively, to elemental tin, $Mn_{1-x}Fe_xSn_2$ ($CuAl_2$-type), $(Mn, Fe)_{2-x}Sn$ (Ni_2In-type) and, in Fe-rich stannides, to $CeNiSi_2$-type $Tm(Mn, Fe)_xSn_2$. All impurities represent $\sim$5 wt. %.

B. Magnetization measurements and neutron diffraction

The thermal variation of the magnetization was measured with a MANICS magnetosusceptometer at a temperature increasing from 300 to 700 K in an applied field of 0.05 T. The low temperature (5–350 K) magnetization measurements were performed upon field cooling with a physical property measurement system (PPMS) from Quantum Design in DC field up to 9 T.

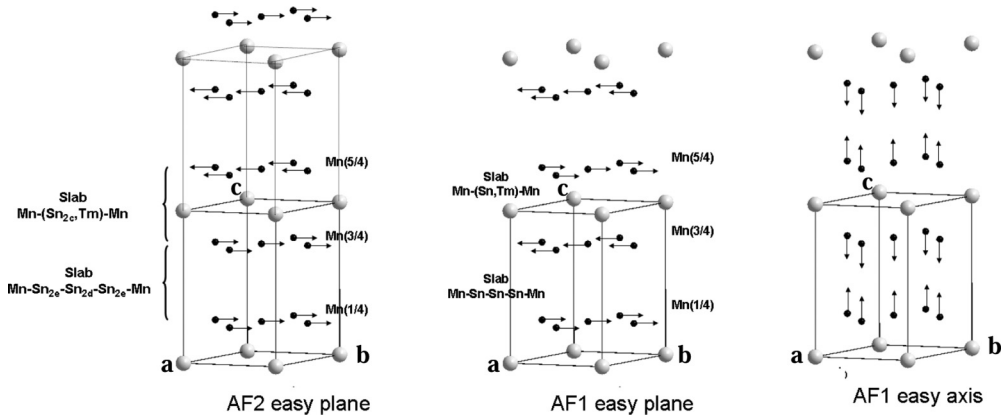

FIG. 2. Magnetic structures of the studied $TmMn_{6-x}Fe_xSn_6$ compounds (further, AFI structures with canted moments are observed in the Fe-rich case, Sn atoms are not shown).

Neutron diffraction patterns were obtained with the D1B diffractometer at the Institut Laue Langevin (Grenoble) at a wavelength $\lambda = 2.520$ Å. Structural and magnetic parameters were refined using FULLPROF software [27]. They are detailed in the Supplemental Material [1].

C. ^{119}Sn Mössbauer spectroscopy

Here, ^{119}Sn Mössbauer spectra were measured in transmission geometry with a spectrometer operating in the conventional constant-acceleration mode. Spectra were recorded at various temperatures from 4.2 to 300 K in a JANIS (Research Company Inc.) liquid helium cryostat. Polycrystalline absorbers, with natural abundance of ^{119}Sn isotope and area density of $\sim 10\,\mathrm{mg\,cm^{-2}}$, were used. The source, kept at RT, was Ba $^{119m}SnO_3$ with a nominal activity of 10 mCi. A palladium foil of 0.05 mm thickness was used as a critical absorber for tin x rays. Velocity calibration was performed against a 12-μm-thick α-Fe foil at RT using a source of ^{57}Co in Rh. Here, ^{119}Sn isomer shifts (ISs or δ) are referred to $BaSnO_3$ at RT.

Here, ^{119}Sn Mössbauer spectra of $TmMn_{6-x}Fe_xSn_6$ were fitted with a standard least-squares method, making assumptions which are briefly described in Sec. IV A in the Supplemental Material [1]. A hyperfine magnetic field distribution was calculated for $TmMSn_6$ at 4.2 K (Sec. X B in the Supplemental Material [1]) with a constrained Hesse-Rübartsch method [28]. In $TmMSn_6$ (M = Mn or Fe), point symmetries at sites 2c, 2d, and 2e, are, respectively, $\bar{6}m2$, $\bar{6}m2$, and $6mm$. They imply that the Z principal axes of the electric field gradient tensors (h = c, d, e) are parallel to the c axis and that the associated asymmetry parameters are all equal to zero (Sec. IV B in the Supplemental Material [1]). The effects of electric field gradients on the fitted hyperfine magnetic fields are further discussed in Sec. IV B in the Supplemental Material [1].

Only absolute values of ^{119}Sn hyperfine magnetic fields were measured in our experimental conditions. These measured fields are the only hyperfine parameters we discuss in this paper. Theoretical results are available for hyperfine magnetic fields transferred at Sn sites in RMn_6Sn_6 with R = Mg, Zr, Hf [17] and for $LiMn_6Sn_6$ [13]. We infer from this information the signs of the measured hyperfine magnetic fields.

III. CRYSTALLOGRAPHIC FEATURES OF $TmMn_{6-x}Fe_xSn_6$

The hexagonal $HfFe_6Ge_6$-type structure (space group no 191: $P6/mmm$) depicted in Fig. 1 may be made from two distinct slabs. The latter are characterized by rather different magnetic interactions in ternary RMn_6Sn_6 stannides [20]: a Mn-[R-Sn(2c)]-Mn slab and a Mn-Sn(2e)-Sn(2d)-Sn(2e)-Mn one [Fig. 1(a)]. The Sn(2d) and Sn(2c) sites are in mirror planes perpendicular to the c axis. Hereafter, tin atoms will be denominated indifferently as Sn($2h$) "atoms" or "sites" where h = c, d, e refers to the sites they occupy (2c, 2d, 2e) (Fig. 1).

Tin atoms at (2c) and (2d) sites in RMn_6Sn_6 are at the centers of trigonal prisms of Mn atoms [Fig. 1(b)]. Their first Mn neighbors form equilateral triangles in two parallel kagome planes. By contrast, the neighbors of Sn(2e) atoms are located at the vertices of regular hexagons of a single kagome plane, as sketched in Fig. 1(b). In $RMn_{6-x}Fe_xSn_6$, all three tin sites have six M transition metal atoms as first nearest neighbors, and the 2c, 2d, and 2e Sn sites have 3, 0, and 1 R neighbors, respectively. These structural features have, among others, the following two consequences:

(a) Only Sn(2e) and Tm atoms contribute significantly to the structure factors of (h k $2l + 1$) lines. They are, for instance, proportional to $(f_{Sn} - f_{Tm})$ for $l = 0$ for any x. Because the coherent scattering lengths b_{Sn} and b_{Tm} have similar values, 6.225 fm and 7.07 fm, respectively, substantial intensities of the (h k 1) neutron diffraction lines are essentially due to magnetic contributions.

(b) The ^{119}Sn hyperfine magnetic fields at the three tin sites depend on the local configurations of the magnetic moments of their first M nearest neighbors, located in two kagome planes for Sn(2d) and Sn(2c) sites and in a single kagome plane for Sn(2e) sites (Fig. 1). Although the two former planes are undistinguishable, we choose for convenience to denote as K^+ the kagome plane first met when going from a given Sn($2h$) atom (h = c, d) in the [001] direction and as K^- the one first met in the opposite direction (Fig. S5 in the Supplemental Material [1]).

Rietveld refinements of XRD patterns (CuKα) of the studied $TmMn_{6-x}Fe_xSn_6$ stannides reveal a slight understoichiometry in Tm ($\approx$5%) within the Fe-rich alloys (Table S2 in the Supplemental Material [1]), which is reminiscent of that observed in the ternary $TmFe_6Sn_6$ parent stannide [25].

IV. MAGNETIC PROPERTIES OF $TmMn_{6-x}Fe_xSn_6$

Figure 3 shows the thermal variation of the magnetization of $TmMn_{6-x}Fe_xSn_6$ stannides, either Mn-rich (x = 0.4, 0.6, 1.2) or Fe-rich (x = 4.25, 4.5, 5.0). Table S3 in the Supplemental Material [1] gives values of some magnetic characteristics of these stannides. Néel temperatures are clearly evidenced in Mn-rich stannides through pronounced local maxima that are much more marked than in Fe-rich stannides. The magnetization jump observed $\sim$270 K in Mn-rich stannides arises from the ferromagnetic $(Mn, Fe)_{2-x}Sn$ impurity. The low-temperature thermal variations of the magnetization of $TmMn_{6-x}Fe_xSn_6$ alloys are presented in Fig. 3(b). Here, $TmMn_{5.4}Fe_{0.6}Sn_6$ shows a two-step increase of the magnetization upon cooling, while $TmMn_{4.8}Fe_{1.2}Sn_6$ displays a pronounced ferromagnetic transition. In contrast, the other stannides show only minor magnetization changes at low temperature. The magnetization curves of $TmMn_{5.6}Fe_{0.4}Sn_6$ and $TmMn_{1.75}Fe_{4.25}Sn_6$ comprise a smooth peak $\sim$25 K. In addition, a slope change occurs $\sim$8 K for $TmMn_{1.5}Fe_{4.5}Sn_6$ and $TmMn_{1.75}Fe_{4.25}Sn_6$.

The field dependences of the magnetization at 4.2 K are shown in Fig. 3(c) for the six studied stannides. They were measured immediately after recording the isofield data. The curves of the alloys with $x = 0.4$ and 0.6 are characterized by a marked irreversible upturn at a critical field close to $\mu_0 H_{crit} \sim 0.9$ T and by a nonzero remnant magnetization. This is likely due to the anisotropy of the magnetically ordered Tm sublattice. The $TmMn_{4.8}Fe_{1.2}Sn_6$ stannide exhibits a spontaneous magnetization, suggesting that $\mu_0 H_{crit}$

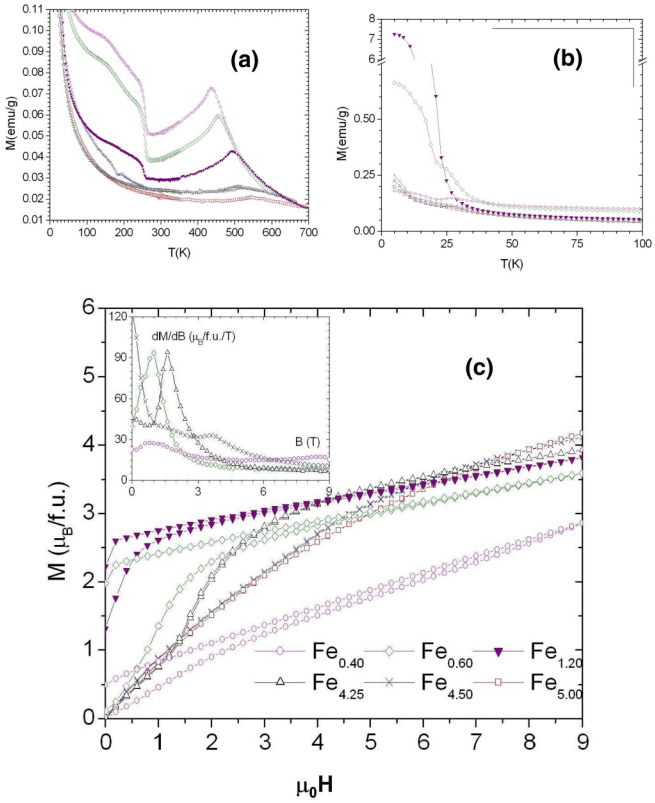

FIG. 3. Thermal variation of the magnetization of $TmMn_{6-x}Fe_xSn_6$ (μ_0Happl = 0.05 T): (a) full temperature range and (b) low-temperature range. (c) Field dependence of magnetization at 4.2 K.

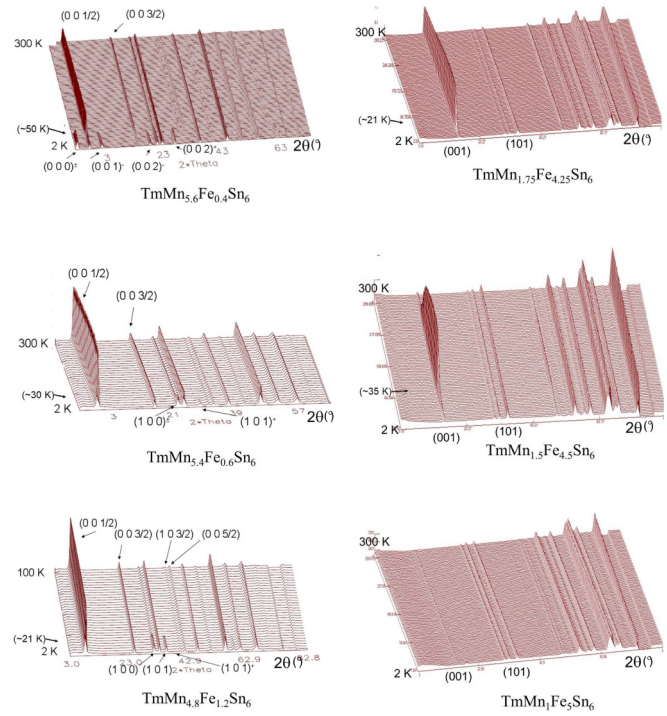

FIG. 4. Thermal evolutions of the neutron diffraction patterns of Mn-rich $TmMn_{6-x}Fe_xSn_6$ compounds ($x = 0.4, 0.6, 1.2$) and of Fe-rich $TmMn_{6-x}Fe_xSn_6$ compounds ($x = 4.25, 4.5, 5.0$).

would be <0.05 T, the field under which the thermomagnetization data were recorded. The three Fe-rich stannides do not exhibit any remnant magnetization, but the curves of $TmMn_{1.75}Fe_{4.25}Sn_6$ and $TmMn_{1.5}Fe_{4.5}Sn_6$ display a pronounced reversible field-dependent transition. This suggests field-induced modifications in the M sublattice.

V. NEUTRON DIFFRACTION

A. Mn-rich $TmMn_{6-x}Fe_xSn_6$ stannides

Figure 4 shows the thermal evolution of the neutron diffraction patterns of the three Mn-rich $TmMn_{6-x}Fe_xSn_6$ solid solutions ($x = 0.4, 0.6, 1.2$).

At high temperature, >∼20–50 K, the three patterns display only the (0 0 $\frac{1}{2}$) and (0 0 $\frac{3}{2}$) peaks characteristic of the AFM AFII structure in addition to the nuclear peaks. The AFII structure is built upon ferromagnetic kagome layers with the moments in the kagome plane (Fig. 2). The interlayer coupling is ferromagnetic through the M-Sn(2e)-Sn(2d)-Sn(2e)-M slab and AFM through the M-[Tm-Sn(2c)]-M, yielding the + + − − sequence (i.e., a magnetic cell twice as large as the chemical one along the c axis). This structure, which occurs only >324 K in $TmMn_6Sn_6$ [24], is thus stabilized by the substitution of Mn with Fe in Mn-rich solid solutions. The refined parameters near $T \sim 90$ K are given in Table S4 in the Supplemental Material [1], while the corresponding neutron patterns are shown in Fig. S4 in the Supplemental Material [1]. Near $T \sim 90$ K, the M moment magnitude refines to $\mu_M \sim 2.2\,\mu_B$, as generally observed in Mn- or Fe-based 1-6-6 stannides [16,17,20,21]. The refined Fe content is close to the nominal one.

The features of the low-temperature patterns strongly depend on the Fe content (Fig. 4). They are related to the magnetic ordering of the Tm sublattice. The diffraction patterns arise from a mixture of several magnetic phases. Because the study of ^{119}Sn hyperfine magnetic fields (Sec. VI) only deals with magnetic structures where only the M sublattice is ordered, the detailed analysis of the low-temperature neutron diffraction patterns is beyond the scope of this paper. We limit ourselves to a brief comment on these patterns (Fig. 4).

Upon cooling <∼20 K, the patterns of $TmMn_{4.8}Fe_{1.2}Sn_6$ mainly display an increase of the (1 0 0) and (1 0 1) peak intensities and the emergence of an additional peak without significant change in the intensity of the (0 0 $\frac{1}{2}$) and (0 0 $\frac{3}{2}$) peaks. The additional peak can be indexed as a $(101)^+$ satellite with a propagation vector (0 0 $q_z \approx 0.34$). Upon cooling, the neutron patterns of $TmMn_{5.4}Fe_{0.6}Sn_6$ also show the appearance of incommensurate peaks without significant change in the intensity of the AFII peaks but with no magnetic intensity on the top of the (1 0 1) nuclear peaks. We observe the successive growths of the $(1\,0\,1)^+$ satellite ($q_z \approx 0.28$) below approximately $T = 29$ K and of the $(101)^+$ satellite ($q_z \approx 0.24$) below approximately $T = 20$ K. This feature is likely related to the two-step variation of the magnetization at low temperature (Fig. 3). By contrast, the low-temperature patterns <∼50 K of $TmMn_{5.6}Fe_{0.4}Sn_6$ are characterized by a strong reduction of the intensities of the AFII peaks

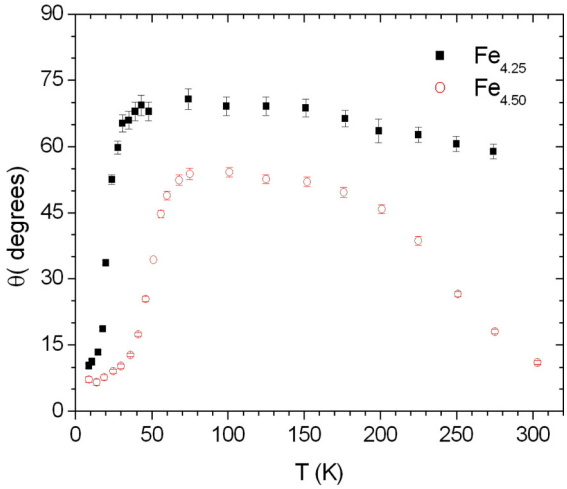

FIG. 5. Temperature dependence of the refined angle θ between the moment direction and the c axis for $TmMn_{6-x}Fe_xSn_6$ with $x =$ 4.25 and 4.50.

concomitant with the growth of a set of magnetic satellites that can be indexed with a propagation vector $(0\ 0\ q_z \approx 0.24)$.

B. Fe-rich $TmMn_{6-x}Fe_xSn_6$ stannides

The thermal evolutions of neutron diffraction patterns of the three Fe-rich $TmMn_{6-x}Fe_xSn_6$ solid solutions ($x = 4.25$, 4.5, 5.0) are shown in Fig. 4.

No superlattice lines are observed. All diffraction peaks can be indexed based on the $HfFe_6Ge_6$-type cell. All patterns are characterized by a significant intensity of the (1 0 1) line, though the corresponding nuclear structure factor is very weak (see Sec. III). This line is characteristic of the AFI AFM structure usually adopted by the Fe moments in RFe_6Sn_6. This structure consists of ferromagnetic kagome planes stacked along the c axis with the $+ - + -$ sequence (Fig. 2). The missing (0 0 1) peak in $TmMn_{1.0}Fe_{5.0}Sn_6$ indicates that the magnetic moment is aligned along the c axis. In contrast, the patterns of the two other Fe-rich stannides ($x = 4.25$ and 4.50) show that the (0 0 1) intensities vary strongly with temperature. These variations show that the moment direction deviates markedly from the c axis. The refinements were carried out with a variable angle θ between the direction of the moments and the c axis. The temperature dependence of the angle θ is presented in Fig. 5. The refined parameters and R factors are given in Table S5 in the Supplemental Material [1], while the observed and calculated patterns are shown in Fig. S5 in the Supplemental Material [1].

The patterns of the three Fe-rich stannides do not exhibit any additional significant change at low temperature, suggesting that the Tm sublattice is not ordered, at least >1.6 K, as in $TmFe_6Sn_6$ [25]. Therefore, the weak low-temperature anomalies in their magnetization curves (Fig. 3) are due to magnetic impurities (Sec. IV).

VI. ^{119}Sn HYPERFINE MAGNETIC FIELDS IN $RMn_{6-x}Fe_xSn_6$ (R = rare earth)

Random vectors are denoted hereafter in bold underlined italic fonts, while their realizations are in bold italic fonts. The hyperfine magnetic field model, which is described below, was first successfully applied to ^{119}Sn hyperfine magnetic fields measured in distannides MSn_2 (M = Mn, Fe) [29–33]. They were seen later to be consistent with theoretical results outlined below.

A. Some literature results about ^{119}Sn transferred hyperfine magnetic fields in $HfFe_6Ge_6$-type RMn_6Sn_6 stannides

Explanations of the various contributions to the ^{119}Sn hyperfine magnetic fields in $HfFe_6Ge_6$-type RMn_6Sn_6 stannides (R = Li, Mg, Zr, Hf) were obtained from first-principles electronic structure calculations [13,17]. Hybridization between metalloid p states and transition metal d states leads to bonding and antibonding hybrids situated at the bottom and at the top of the transition metal d band, respectively [17]. The s symmetry states of Sn atoms exhibit two regions with different polarization signs, going from negative at low energy to positive at an energy larger than the Fermi energy. Bonding states with a preferential occupation by minority spin states corresponds to the low-energy part, while the reverse holds for antibonding states at higher energy. The total Fermi contact contribution, which arises from the finite spin density of 5s electrons at ^{119}Sn nuclei, is the sum of a negative contribution due to the bonding states and of a positive contribution due to the antibonding states. Theoretical calculations show that the transferred hyperfine magnetic fields in the previous RMn_6Sn_6 stannides are negative, i.e., their directions are opposite to the directions of the magnetic moments of the first Mn neighbors (or to the directions of their sums) [17].

In addition to the Fermi contact term, transferred hyperfine magnetic fields include a negligible orbital contribution [17] and a small lattice dipolar contribution (<1 T), due to the moments of neighboring atoms. The transferred hyperfine magnetic fields include also a local dipolar contribution arising from the nonspherical valence p spin density of tin hybridized with the spin-polarized d states of transition metal atoms. The latter dipolar part of the transferred field, which is simply explained as being due to the spin density of valence p electrons localized in each Mn-Sn bond, can be as large as several Tesla for Sn atoms. The lattice dipolar field due to the first nearest magnetic moments and the previous local dipolar field are formally identical. A hand-waving argument is as follows: the local term defined above is by far larger than the lattice term because of the typical r^{-3} distance dependence of dipolar fields. The dipolar field we consider is represented by the left term of Eq. (1). A priori, it is not collinear with the contact field.

Both the separation between bonding and antibonding states and the 5s spin polarization increase when the Mn-Sn distance decreases. The M-Sn(2h) distances at 300 K, for h = c, d, e, in $TmMn_{6-x}Fe_xSn_6$ stannides studied herein, are respectively ≈2.57, 2.61, and 2.86 Å in Mn-rich stannides and ≈2.57, 2.56, and 2.80 Å in Fe-rich stannides, for any x in the two investigated Fe ranges. Thus, the measured hyperfine magnetic field at the Sn(2e) site is expected to be smaller than those measured at Sn(2d) and/or at Sn(2c) sites. However, this occurs only if the sums of the first M nearest neighbor moments of the last two sites differ from zero [Eq. (1) below].

B. An explicit simple model of ^{119}Sn transferred hyperfine magnetic fields applied to various stannides

The present study of hyperfine magnetic fields in stannides, with a $HfFe_6Ge_6$-type structure, is restricted to "high" temperatures for which only M (Mn, Fe) magnetic moments are ordered. The studied stannides with AFI and AFII structures might be looked at as "pseudo-binary alloys" of Mn and Fe atoms in parallel kagome planes, probed locally by ^{119}Sn atoms. The ^{119}Sn hyperfine magnetic fields $\boldsymbol{B}_M^{(2h)}$ in $TmMn_{6-x}Fe_xSn_6$ pseudobinary alloys are modeled by Eq. (1). On the left is a vector sum of anisotropic dipolar hyperfine magnetic fields, and on the right is a vector sum of Fermi contact isotropic hyperfine magnetic fields, both due to the six M first nearest neighbors of the considered tin site:

$$\boldsymbol{B}_M^{(2h)} = \sum_{i=1}^{6} A_{aMi}(2h)\left[\boldsymbol{u}_{Mi}(\boldsymbol{\mu}_{Mi}\cdot\boldsymbol{u}_{Mi}) - \frac{1}{3}\boldsymbol{\mu}_{Mi}\right] + \sum_{i=1}^{6} A_{isMi}(2h)\boldsymbol{\mu}_{Mi}. \quad (1)$$

The hyperfine magnetic fields we measured are the moduli of $\boldsymbol{B}_M^{(2h)}$. The conversion constants $A_{aMi}(2h)$, $A_{isMi}(2h)$, (h = c, d, e), from magnetic moments into, respectively, anisotropic and isotropic hyperfine magnetic fields depend on the studied stannide, on the considered tin site, and on the nature of its ith M nearest neighbor. Figure S5 in the Supplemental Material [1] exemplifies some constituents of Eq. (1). As mentioned above, the ^{119}Sn hyperfine magnetic fields are negative in $HfFe_6Ge_6$-type RMn_6Sn_6 stannides [17], as are then the isotropic coefficients $A_{isMn}(2h)$.

C. Anisotropic and isotropic constants in $HfFe_6Ge_6$-type RMn_6Sn_6 stannides

The anisotropic fractions of the total transferred hyperfine magnetic fields are measured to be almost negligible fractions, ∼3 to 4%, of the total hyperfine magnetic fields for Sn(2d) and Sn(2c) sites in $RMn_6Sn_{6-x}X_x$ (R = Y, Tb, Er, and X = In, Ga) [21]. As the hyperfine magnetic fields are negative (Sec. VI A), the $A_{aMn}(2h)$ and the $A_{isMn}(2h)$, which have the same sign for all Sn sites [21], are negative.

In a series of 14 RMn_6Sn_6 stannides with ferromagnetically coupled Mn moments in (001) kagome planes, transferred hyperfine magnetic fields at Sn(2d) sites range from 30 to 33.4 T at $T \leqslant 7$ K. In these stannides, R atoms are not all rare earth elements (R = Li, Mg, Zr, Hf, Sc, Y, Gd, Tb, Dy, Ho, Er, Tm, Yb, Lu [13,17,18]). Further, Mn magnetic moments have similar values at low temperature, $\mu_{Mn} \sim 2.5(3)\mu_B$, and similar relative orientations. This rather narrow distribution of hyperfine magnetic fields is consistent with the smallness of anisotropic constants as compared with isotropic constants. Although large, the previous hyperfine magnetic fields are much smaller than the one of 57 T measured at ^{119}Sn impurities on Gd sites in hexagonal $GdCo_5$ at 5 K [34].

D. Additional assumptions about $A_{isM}(2h)$ and $A_{aM}(2h)$ constants in $TmMn_{6-x}Fe_xSn_6$

The lack of experimental or theoretical information about possible local distortions produced by the substitution of Mn with Fe in $TmMn_{6-x}Fe_xSn_6$ pseudobinary alloys, particularly in the Fe-rich range, leads us to make additional assumptions on the parameters associated with the six Sn($2h$)-M bonds of any tin site:

(a) The anisotropic and isotropic constants $A_{aMn}(2h)$ and $A_{isMn}(2h)$ are supposed to be identical for all Sn($2h$)-Mn bonds, as are $A_{aFe}(2h)$ and $A_{isFe}(2h)$ for all Sn($2h$)-Fe bonds. The latter are a priori different from the former, and all may depend on x.

(b) All the projections of unit vectors carried by Sn($2h$)-Mn bonds (Fig. 1 and Fig. S5 in the Supplemental Material [1]) on the c axis are assumed to have the same lengths. The same assumption holds for all the projections onto the ab plane. Similar assumptions apply to all Sn($2h$)-Fe bonds, but the lengths differ a priori from the previous ones. These lengths are denoted, respectively, as $u_{zM}(2h)$ (c axis) and $u_{abM}(2h)$ (ab plane).

Experimental hyperfine magnetic fields (Sec. VIII) suggest that anisotropic and isotropic constants differ for Mn- and Fe-rich stannides. However, as x/6 varies only by ∼0.13 and ∼0.29 in Mn- and Fe-rich stannides, respectively, the previous constants are seen to be essentially independent of x in each range. Finally, the projections of the above unit vectors may vary, though moderately, with temperature, at most 300 K.

E. Probabilities of configurations of M atoms around Sn atoms in $TmMn_{6-x}Fe_xSn_6$

Here, Sn($2h$), (h = c, d, e), have all six M first nearest neighbors. For a random distribution of M atoms on kagome lattices, the probability $P(p)$ that a Sn($2h$) atom [named hereafter Sn_{2h}(p)] has p Fe atoms and 6-p Mn atoms as nearest neighbors is simply given by a classical binomial distribution which is written as

$$P(p) = \binom{6}{p}\left(\frac{x}{6}\right)^p\left(1-\frac{x}{6}\right)^{6-p} \quad (p = 0, 1, ..., 6), \quad (2)$$

where $\binom{6}{p}$ is a binomial coefficient. Table S6 in the Supplemental Material [1] gives the most significant values of $P(p)$ for the different pseudobinary alloys we studied. The number of configurations of p Fe neighbors of Sn(2c) or Sn(2d) atoms contained in a single kagome plane $A^{(1)}(p)$ or in two kagome planes $A^{(2)}(p)$ is further given in Table S7 in the Supplemental Material [1].

VII. PREDICTED ^{119}Sn HYPERFINE MAGNETIC FIELDS IN $RMn_{6-x}Fe_xSn_6$ STANNIDES

The considered magnetic structures are described from a stacking of parallel kagome planes, each with ferromagnetically coupled transition metal atoms M (Secs. V A and V B), whose moment magnitudes μ_M are either equal to μ_{Mn} or to μ_{Fe}.

A. General expressions of hyperfine magnetic fields in RM_6Sn_6

1. Anisotropic hyperfine magnetic fields in RM_6Sn_6

The contribution of K^+ to anisotropic hyperfine magnetic fields at Sn($2h$) sites $\boldsymbol{B}_{aM}^{(2h)}(K^+)$ is calculated in Sec. V A in the Supplemental Material [1] from the left sum in Eq. (1) to be

$$\boldsymbol{B}_{aM}^{(2h)}(K^+) = A_{a\text{eff},M}(2h)\left[\frac{\alpha(2h)}{2}\right](\boldsymbol{\mu}_M - 3\boldsymbol{\mu}_{zM}), \quad (3)$$

where $\alpha(2h) = 1, 1, 2$ for $h =$ c, d, e, respectively, and $\boldsymbol{\mu}_{zM}$ is the projection of the magnetic moment $\boldsymbol{\mu}_M$ on the [001] axis. Further, $A_{a\text{eff},M}(2h) = A_{aM}(2h)[1-3u_{zM}^2(2h)]$, where $u_{zM}^2(2h)$ is the square of the length of the projection on the c axis of a unit vector carried by any Sn($2h$)-M bond.

2. Total hyperfine magnetic fields in RM_6Sn_6 (M is either Mn or Fe)

The moments $\boldsymbol{\mu}_M$ of M atoms, in a single kagome plane or in two successive kagome planes, are assumed to make an angle θ with the c axis at a temperature T made explicit in Eqs. (4) and (5). The latter equations hold for those Sn($2h$) sites which are sandwiched between two ferromagnetically coupled kagome planes and, in all cases, for Sn(2e) sites which are bound to a single plane. In addition to $h =$ e,

(a) $h =$ c, d in ferromagnetic RM_6Sn_6 stannides (examples are given in Ref. [21]), and

(b) $h =$ d in RM_6Sn_6 stannides with the AFII AFM structure (Fig. 2).

An orthonormal coordinate system with unit vectors ($\boldsymbol{u}_x$, $\boldsymbol{u}_y$, $\boldsymbol{u}_z$), where $\boldsymbol{u}_z = [001]$ (Fig. S5 in the Supplemental Material [1]), is defined in Sec. V in the Supplemental Material [1]. The total angle-dependent hyperfine magnetic fields at Sn($2h$) sites defined above at a temperature T, $\boldsymbol{B}_{M,T}^{(2h)}(\theta)$, are obtained in the ($\boldsymbol{u}_x$, $\boldsymbol{u}_y$, $\boldsymbol{u}_z$) reference system from Eqs. (1) and (3) to be

$$\boldsymbol{B}_{M,T}^{(2h)}(\theta) = B_{M,T}^{(2h)}(90^\circ)\sin\theta\boldsymbol{u}_x + B_{M,T}^{(2h)}(0^\circ)\cos\theta\boldsymbol{u}_z. \quad (4)$$

Equation (4) and some of its applications are discussed in Sec. V B in the Supplemental Material [1]. For Sn atoms, with six identical nearest neighbors ($M =$ Mn or Fe), Eqs. (1) and (3) yield the explicit expressions of $B_{M,T}^{(2h)}(90^\circ)$ and $B_{M,T}^{(2h)}(0^\circ)$ as

$$\theta = 90^\circ \Rightarrow B_{M,T}^{(2h)}(90^\circ) = [6A_{isM}(2h) + A_{a\text{eff},M}(2h)]\mu_M(T)$$
$$\theta = 0^\circ \Rightarrow B_{M,T}^{(2h)}(0^\circ) = [6A_{isM}(2h) - 2A_{a\text{eff},M}(2h)]\mu_M(T). \quad (5)$$

In general, the direction of the total hyperfine magnetic field, calculated from Eq. (1), deviates from the moment direction in collinear magnetic structures except if they are easy plane or easy axis (Fig. 2).

B. Hyperfine magnetic fields in stannides $TmMn_{6-x}Fe_xSn_6$

Hyperfine magnetic fields at tin sites in $TmMn_{6-x}Fe_xSn_6$ change when 6 Mn neighbors are replaced by 6-p Mn neighbors and p Fe neighbors ($p = 0, \ldots, 6$). Therefore, the vector hyperfine magnetic field at a given tin site Sn($2h$) is a random vector $\boldsymbol{B}_M^{(2h)}$, which takes a set of vector values associated with the many possible ways of distributing 6 Mn and Fe first nearest neighbors around the given tin site for the given Fe content.

The anisotropic hyperfine magnetic field $\underline{\boldsymbol{B}_{aM}^{(2h)}}$ is a sum of six random vectors $\underline{\boldsymbol{X}_{Mi}}$ ($i = 1, \ldots, 6$) associated with dipolar hyperfine magnetic fields (HMFs). The two possible values of each of the 6 $\underline{\boldsymbol{X}_{Mi}}$ are $\boldsymbol{X}_{Mi} = A_{aMi}(2h)[\boldsymbol{u}_{Mi}(\boldsymbol{\mu}_{Mi}\cdot\boldsymbol{u}_{Mi}) - \boldsymbol{\mu}_{Mi}/3]$, where Mi is either Mn or Fe [Eq. (1)]. The random hyperfine magnetic field at site Sn($2h$) is then $\underline{\boldsymbol{B}_M^{(2h)}} = \sum_{i=1}^{6}[\underline{\boldsymbol{X}_{Mi}} + A_{isMi}(2h)\underline{\boldsymbol{\mu}_{Mi}}]$, where the last term is the isotropic hyperfine magnetic field which depends on a random magnetic moment $\underline{\boldsymbol{\mu}_{Mi}}$ either equal to $\boldsymbol{\mu}_{Mni}$ or to $\boldsymbol{\mu}_{Fei}$. Further calculations are described in Sec. VI A in the Supplemental Material [1].

For those Sn($2h$) atoms which have either 6 Mn or 6 Fe first nearest neighbors, the magnetic hyperfine fields we consider have well-defined values. For M being either Mn or Fe everywhere in the next three relations, we write the anisotropic fields from Eq. (1)

$$\boldsymbol{B}_{aM}^{(2h)} = \sum_{i=1}^{6} A_{aM}(2h)\left[\boldsymbol{u}_i(\boldsymbol{\mu}_M\cdot\boldsymbol{u}_i) - \frac{\boldsymbol{\mu}_M}{3}\right] = \sum_{i=1}^{6}\boldsymbol{X}_{Mi}, \quad (6)$$

the isotropic fields $\boldsymbol{B}_{isM}^{(2h)} = 6A_{isM}(2h)\boldsymbol{\mu}_M$, and the total hyperfine magnetic fields

$$\boldsymbol{B}_M^{(2h)} = \boldsymbol{B}_{aM}^{(2h)} + \boldsymbol{B}_{isM}^{(2h)}. \quad (7)$$

All sites (6i) occupied at random by M atoms in $TmMn_{6-x}Fe_xSn_6$ are statistically equivalent. However, from the point of view of tin "probes," the statistical equivalency of their 6 M first nearest neighbors depends further on local magnetic structures. The assumptions done in Sec. VI D lead us to distinguish two main cases, relevant for the AFI and AFII magnetic structures, for which the six first nearest neighbor sites of the considered tin atoms are

(1) statistically equivalent. This is the case for Sn(2e) sites whose 6 M first nearest neighbors are always ferromagnetically coupled and are thus interchangeable. This is also the case of tin sites sandwiched between two ferromagnetically coupled kagome planes [case (a) of Sec. VII A 2]; or

(2) statistically inequivalent. This holds for tin sites sandwiched between two kagome planes, which are not themselves ferromagnetically coupled. The six neighboring sites are then split into two groups of three equivalent sites, each in a ferromagnetic kagome plane. Then it is necessary to know not only the total number p of Fe first nearest neighbors but also their repartition among the two neighboring kagome planes (p_1, p_2).

For a given Fe content x and a random substitution of Mn atoms with Fe atoms, the average hyperfine magnetic fields at Sn($2h$) atoms are calculated in Sec. VI in the Supplemental Material [1] as a function of p [and if required of (p_1, p_2)]. A comparison of experimental fields with the moduli of their calculated counterparts is thus possible.

1. Six statistically equivalent first nearest neighbor sites

Experimental results (Sec. VIII) show only a weak hyperfine magnetic field dependence on x for a given number p of their Fe nearest neighbors for stannides which belong to the same class, i.e., either to the Mn- or Fe-rich class. The calcu-

lated average hyperfine magnetic fields $\boldsymbol{B}_M^{(2h)}(p)$ (x is omitted) yield predicted hyperfine magnetic fields $B_{\rm pred}^{(2h)}(p)$, the modulus of $\boldsymbol{B}_M^{(2h)}(p)$ which are just those to which experimental hyperfine magnetic fields $B_{\rm exp}^{(2h)}(p)$ have to be compared.

With the set of assumptions described in Sec. VI D, the average anisotropic and isotropic hyperfine magnetic fields and thus the average total hyperfine magnetic fields at sites $Sn_{2h}(p)$, where p is a fixed number, are calculated in Sec. VI A in the Supplemental Material [1]. Equations (24)–(26) in the Supplemental Material [1] give explicitly the separate anisotropic (subscript aM) and isotropic (isM) contributions to the total (M) hyperfine magnetic field of Sn($2h$) atoms which have p Fe first nearest neighbors $\boldsymbol{B}_{aM}^{(2h)}(p)$, $\boldsymbol{B}_{isM}^{(2h)}(p)$, and $\boldsymbol{B}_M^{(2h)}(p)$. The average total field (Eq. (26) in the Supplemental Material [1])

$$\boldsymbol{B}_M^{(2h)}(p) = \boldsymbol{B}_{\rm Mn}^{(2h)} - p\frac{\left[\boldsymbol{B}_{\rm Mn}^{(2h)} - \boldsymbol{B}_{\rm Fe}^{(2h)}\right]}{6} \qquad (8)$$

is then a weighted sum, linear in p, of the two hyperfine magnetic fields $\boldsymbol{B}_{\rm Mn}^{(2h)}$ and $\boldsymbol{B}_{\rm Fe}^{(2h)}$ [Eq. (7)] of Sn($2h$) atoms with, respectively, 6 Mn and 6 Fe first nearest neighbors. Ideally, the latter fields are or would have to be measured both at the same temperature for the given Fe content.

2. *Two groups of three statistically equivalent first nearest neighbor sites*

For Sn($2h$) atoms sandwiched between two kagome planes AFM coupled, the index h is $h =$ c, d for the AFI structure, while it is $h =$ d for the AFII structure (Fig. 2). The numbers of Fe atoms in kagome planes K^- and in K^+ (Fig. S5 in the Supplemental Material [1]) are denoted, respectively, as p_1 and $p_2 = p - p_1$ (Table S7 in the Supplemental Material [1]). In easy-axis AFI and easy-plane AFII, the isotropic and anisotropic contributions to total hyperfine magnetic fields are collinear. Further, if the anisotropic hyperfine magnetic fields are negligible as compared with the isotropic ones, then the predicted experimental hyperfine magnetic fields reduce to (Eq. (28) in the Supplemental Material [1])

$$B_{\rm pred}^{(2h)}(N_{\rm Fe}) = N_{\rm Fe}|A_{is\rm Mn}(2h)\mu_{\rm Mn} - A_{is\rm Fe}(2h)\mu_{\rm Fe}|, \qquad (9)$$

where $N_{\rm Fe} = |p_2 - p_1|$ plays the role of an "effective" number of Fe nearest neighbors. Relations, which include anisotropic terms, are given in Sec. VI B in the Supplemental Material [1]. In all cases, the calculated hyperfine magnetic fields vary linearly with $N_{\rm Fe}$.

Finally, the dispersion of the distribution of the modulus of the random magnetic hyperfine field $\boldsymbol{B}_M^{(2h)}$ contributes to Mössbauer line broadening, possibly asymmetrical to some extent.

VIII. EXPERIMENTAL ^{119}Sn HYPERFINE MAGNETIC FIELDS of $TmMn_{6-x}Fe_xSn_6$ AND THEIR INTERPRETATION

As we measure only absolute values of hyperfine magnetic fields, we define for convenience $A_{isM}^-(2h) = -A_{isM}(2h)$ and $A_{aM}^-(2h) = -A_{aM}(2h)$ ($M =$ Mn, Fe, $h =$ c, d, e).

Section IV B in the Supplemental Material [1] discusses the validity of hyperfine magnetic fields as obtained from Mössbauer spectra with the assumption that first-order perturbation theory holds. It leads us to conclude that anisotropic and isotropic constants are confidently calculated for tin sites whose hyperfine magnetic fields are large enough. The latter are measured at tin sites whose first nearest neighbors are ferromagnetically coupled, i.e., Sn(2e) in all stannides and Sn(2d) in Mn-rich stannides (easy-plane AFII structure).

A. Three Mn-rich stannides ($x = 0.4, 0.6, 1.2$) in the easy-plane AFII state ($T \geqslant 30$ K)

The easy-plane AFII-type structure (Fig. 2), which exists only >324 K in $TmMn_6Sn_6$ [24], is stabilized by the substitution of Mn with Fe. Figure 6 shows observed and calculated ^{119}Sn Mössbauer spectra of three $TmMn_{6-x}Fe_xSn_6$ stannides with $x = 0.4$, 0.6, and 1.2, recorded respectively at 55, 46, and 30 K in the AFII state, while those observed at 4.2 K, with magnetically ordered Tm moments, are shown in Fig. S6 in the Supplemental Material [1]. All parameters obtained from least-squares fits are collected in Table S8 in the Supplemental Material [1].

Positive ratios $A_{a\rm Mn}(2h)/A_{is\rm Mn}(2h) <\approx 7\%$ in $RMn_6Sn_{6-x}X_x$ compounds ($R =$ Y, Tb, Er; $X =$ In, Ga) are reported in Ref. [21] for Sn(2d) and Sn(2c) sites. They range between ~20 and ~70% for site Sn(2e). The isotropic contribution is thus expected to be still the main part of the total hyperfine magnetic field in Mn-rich stannides. As $A_{is\rm Mn}(2h)$ is negative, $A_{a\rm Mn}(2h)$ is also negative. Both constants are conveniently written as $A_{uM}^-(2h)(u = is, a, a\text{eff})$.

1. *An estimate of $A_{is\rm Mn}^-$(2d) from the hyperfine magnetic fields of* $TmMn_6Sn_6$

The hyperfine magnetic field of Sn(2d) atoms in $TmMn_6Sn_6$, which has thus 6 Mn neighbors ($p = 0$), $B_{\rm exp}^{(2d)}(0)$, lies most likely between 30 and 33.4 T. Indeed, Table S8 in the Supplemental Material [1] shows that the measured $B_{\rm exp}^{(2d)}(0)$ appear to be independent of x, with a mean of 31.3 ± 0.3 T at temperatures of 30, 46, and 55 K. The latter mean is 31.7 ± 0.3 T at 4.2 K. All these values are close to $B_{\rm exp}^{(2d)}(0) = 32.1(3)$ T measured in $ZrMn_6Sn_6$ at 100 K, which has an AFII magnetic structure >≈70 K, with $\mu_{\rm Mn} = 2.11\mu_{\rm B}$ [17]. The predicted hyperfine magnetic field at Sn(2d) nuclei $B_{\rm pred}^{(2d)}(0)$ is $[6A_{is\rm Mn}^-(2d) + A_{a\text{eff},\rm Mn}^-(2d)]\mu_{\rm Mn}$ ($\theta = 90°$), as deduced from Eq. (5). Neglecting the anisotropic contribution gives $A_{is\rm Mn}^-(2d) = B_{\rm exp}^{(2d)}(0)/(6\mu_{\rm Mn}) = 2.3(3)\text{T}/\mu_{\rm B}$, with $\mu_{\rm Mn} \sim 2.3(3)\mu_{\rm B}$ at 2 K (neutron diffraction) and $B_{\rm exp}^{(2d)}(0) =$ 31.5 T.

2. *Sn(2d) and Sn(2e) atoms in Mn-rich* $TmMn_{6-x}Fe_xSn_6$

Here, $Sn_{2h}(p)$ atoms ($h =$ d, e) with p Fe neighbors are characterized, among others, by their experimental hyperfine magnetic fields $B_{\rm exp}^{(2h)}(p)$ and by their relative areas $f_{2h}(p)$ (Table S6 in the Supplemental Material [1]) or equivalently by their relative fractions.

The sextets with the largest hyperfine magnetic fields ~31.5 T are attributed consistently to Sn(2d) sites with 6 Mn neighbors (Sec. VIII A 1). Sextets with external peaks at ~−18 and ~+21 mm/s are observed for $x = 0.4$, 0.6, and 1.2 but not for $ZrMn_6Sn_6$ (Fig. 6). They are attributed to Sn(2d)

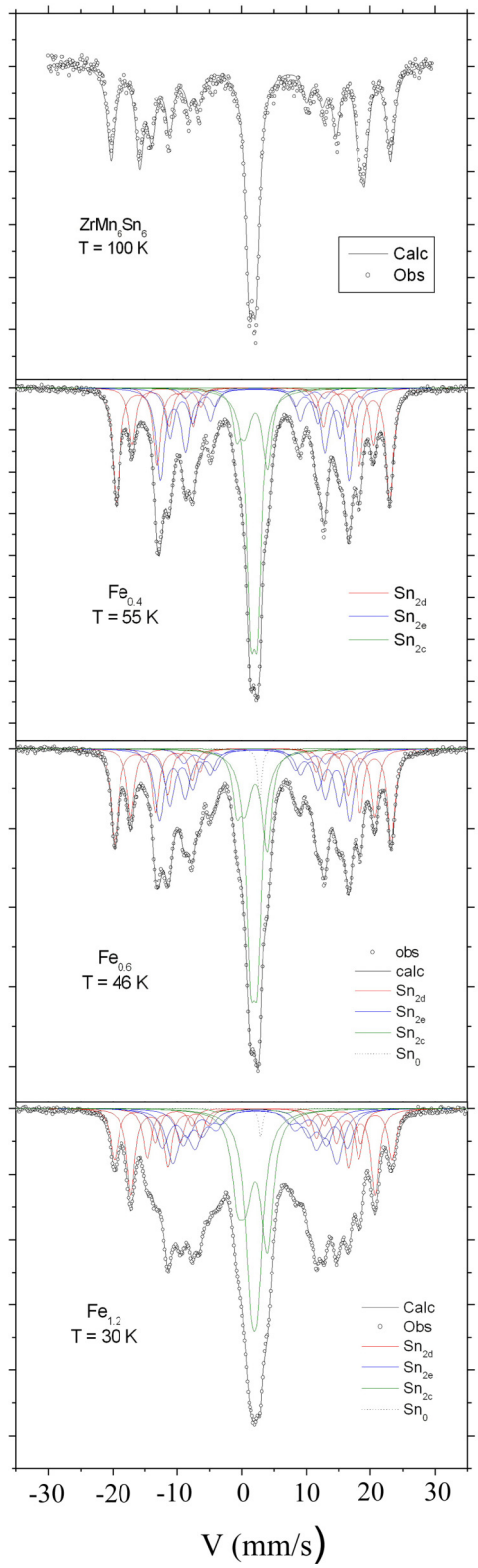

FIG. 6. Observed and calculated ^{119}Sn Mössbauer spectra of (1) $ZrMn_6Sn_6$ at 100 K (top) and (2) $TmMn_{6-x}Fe_xSn_6$ ($x = 0.4$; 0.6; 1.2) with AFII easy-plane structures.

atoms, surrounded by 5 Mn and 1 Fe atoms. Additional sextets are associated with Sn(2d) atoms with 4 Mn and 2 Fe neighbors. The hyperfine magnetic fields $B^{(2d)}_{exp}(p)$ remain almost constant with x for any of the observed values of p. Similarly, the various subspectra associated with Sn(2e) atoms, whose hyperfine magnetic fields range from ∼13 to ∼21 T, are identified notably from a comparison of the variations with x of their relative areas to the expected values.

The hyperfine magnetic field changes with p are predominantly due to isotropic contributions of the six first nearest neighbors of Sn atoms, as suggested by first-principles calculations ([17] and Sec. VI A). We consider first the isotropic contribution where the common direction of M moments is taken as the reference direction. The following equations are formally identical for Sn(2d) and Sn(2e), which have both six ferromagnetically coupled neighbors. The predicted absolute value of the isotropic hyperfine magnetic field for a given Fe content x and a given temperature is deduced from Eq. (24) in the Supplemental Material [1] to be

$$B^{(2h)}_{pred}(p) = B^{(2h)}_{pred}(0) - p\Delta A_{is}(2h), \tag{10}$$

where $\Delta A_{is}(2h) = A^{-}_{isMn}(2h)\mu_{Mn} - A^{-}_{isFe}(2h)\mu_{Fe}$.

In Mn-rich alloys, the predicted hyperfine magnetic fields at $Sn_{2d}(p)$ and $Sn_{2e}(p)$ sites vary linearly with p, in agreement with experiment (Fig. 7). Figure 7 indicates further that the hyperfine magnetic fields are essentially independent of x ($x \leqslant 1.2$).

Table S8 in the Supplemental Material [1] shows that $0 < B^{(2h)}_{exp}(p) < B^{(2h)}_{exp}(0)$ for $h =$ d and e and the values of p whose associated spectral areas are significant ($0 < p \leqslant 3$, $x \leqslant 1.2$). Thus, the $\Delta A_{is}(2h)$ are positive, i.e., $A^{-}_{isMn}(2h)\mu_{Mn} > A^{-}_{isFe}(2h)\mu_{Fe}$ [$A^{-}_{isMn}(2h) > 0$] for Mn-rich stannides. The $Sn_{2d}(p)$ hyperfine magnetic fields are larger than those of $Sn_{2e}(p)$ atoms with slopes $-\Delta A_{is}(2d) = -3.4(1)$T and $-\Delta A_{is}(2e) = -2.5(1)$T. This suggests that the isotropic constants $A^{-}_{isMn}(2e)$ would be at most ∼0.7 $A^{-}_{isMn}(2d)$, as the effect of an anisotropic contribution on the total hyperfine magnetic field would have to be considered for site Sn(2e) [21].

If we take $A^{-}_{isMn}(2d) = 2.3(3)\text{T}/\mu_B$ (Sec. VIII A), then the measured slope yields an estimate of $A^{-}_{isFe}(2d) \sim 0.8\text{T}/\mu_B$ for $\mu_{Fe} = \mu_{Mn} \sim 2.3\mu_B$. The isotropic constant $A_{isFe}(2d)$ obtained in that way is thus negative, as is $A_{isMn}(2d)$.

The effect of an anisotropic contribution on the total hyperfine magnetic field must be considered for site Sn(2e), albeit the isotropic contribution still dominates the total hyperfine magnetic field in Mn-rich stannides all the more that the anisotropic term is $A^{-}_{aeff,M}(2e)/6$ in the definition of $A^{-}_{M}(2e)$ [Eq. (11)]. The latter constant is convenient to express $B^{(2e)}_{pred}(0) = 6A^{-}_{M}(2e)\mu_{Mn}$ from Eq. (5) for $\theta = 90°$. From Eq. (8) and Eqs. (24) to (26) in the Supplemental Material [1], the predicted experimental hyperfine magnetic field is written finally as $B^{(2e)}_{pred}(p) = B^{(2e)}_{pred}(0) - p\Delta A_M(2e)$. We define, for all Sn sites,

$$A^{-}_{M}(2h) = A^{-}_{isM}(2h) + \frac{A^{-}_{aeff,M}(2h)}{6} \quad (\theta = 90°)$$
$$\Delta A_M(2h) = A^{-}_{Mn}(2h)\mu_{Mn} - A^{-}_{Fe}(2h)\mu_{Fe}. \tag{11}$$

The difference between $\Delta A_{is}(2e)$ and $\Delta A_M(2e)$ is that the latter includes both isotropic and anisotropic constants. For a given x, hyperfine magnetic fields at Sn(2e) sites are then predicted to vary linearly with the number p of Fe neighbors, in agreement with experiment (in Tesla) $B^{(2e)}_{exp}(p) = 21.2 - 2.5p$ (Table I, Fig. 7). However, the two experimental values,

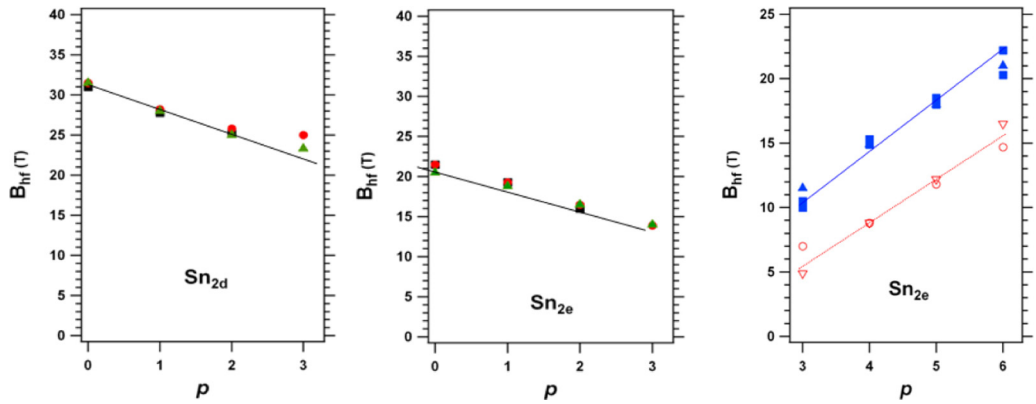

FIG. 7. Measured ^{119}Sn hyperfine magnetic fields (HMFs) on the one hand for sites Sn(2d) and Sn(2e) in Mn-rich $TmMn_{6-x}Fe_xSn_6$ (x = 0.4, 0.6, 1.2) AFII compounds (left and middle figures) and on the other for sites Sn(2e) in Fe-rich (x = 4.25, 4.5) AFI compounds (right figure). Experimental HMFs are plotted vs the number p of Fe neighbors of tin atoms. Line equations are given in Table I.

$B_{\rm exp}^{(2e)}(0)$ and the slope, do not suffice to evaluate the four in number isotropic and anisotropic constants which appear in $\Delta A_M(2e)$ [Eq. (11)], so that only $A_{\rm Mn}^-(2e)$ and $A_{\rm Fe}^-(2e)$ can be evaluated.

In Mn-rich stannides, $A_{\rm Mn}^-(2e) = 21.2/(6\mu_{\rm Mn}) = 1.53(7)\,{\rm T}/\mu_{\rm B}$ is obtained from $B_{\rm exp}^{(2e)}(0)$. From the slope 2.5 T, we calculate further that $A_{\rm Fe}^-(2e) = 0.44(8)\,{\rm T}/\mu_{\rm B}$. Electronic structure calculations [17] show that the negative isotropic terms are dominant in Mn-rich stannides. Thus, $A_{\rm Mn}(2e) = -1.53(7){\rm T}/\mu_{\rm B}$ and (Sec. VIII A) $A_{\rm Fe}(2e) = -0.44(8){\rm T}/\mu_{\rm B}$.

3. Sn(2c) sites

Only qualitative information, further discussed in Sec. VIII B 2 in the Supplemental Material [1], can be derived because the hyperfine magnetic fields of these sites are small, ∼3.5 T (Table S8 in the Supplemental Material [1]), and their quadrupole splittings are large, ∼2 mm/s (Sec. IV B in the Supplemental Material [1]).

TABLE I. ^{119}Sn Mössbauer spectra of $TmMn_{6-x}Fe_xSn_6$ stannides were recorded for the experimental combinations (Fe content x, temperature T) given in the left column. Hyperfine magnetic fields of Sn(2d) and Sn(2e) sites, obtained from these spectra, vary linearly with p, their number of Fe first nearest neighbors (Fig. 7). Equations of the fitted lines are in the middle column and in the right column for Sn(2d) and Sn(2e), respectively. Errors on all parameters range typically from 0.2 to 0.4 T (Mn-rich) and from 0.5 to 1 T (Fe-rich).

$TmMn_{6-x}Fe_xSn_6$ (x, T)	Sn(2d) $B_{\rm exp}^{(2d)}(p)$ (T)	Sn(2e) $B_{\rm exp}^{(2e)}(p)$ (T)
Mn-rich	$0 \leqslant p \leqslant 3$	$0 \leqslant p \leqslant 3$
($x = 0.4$, $T = 55$ K)	$31.2 - 3.4p$	$21.2 - 2.5p$
($x = 0.6$, $T = 46$ K)		
($x = 1.2$, $T = 30$ K)		
Fe-rich		$3 \leqslant p \leqslant 6$
($x = 4.25$, $T = 4.2$ K)		$1.5 + 3.3p$
($x = 4.50$, $T = 4.2$ K)		
($x = 4.25$, 51 K)		$-4 + 3.3p$
($x = 4.50$, 72 K)		
($x = 5$, 4.2 K)		$3.7p$

B. Fe-rich stannides (x = 4.25, 4.5, 5, 6)

Fe-rich stannides have an AFI AFM structure (Fig. 2) observed in a range of Fe content like the one, $x > 3.5$, measured in $ErMn_{6-x}Fe_xSn_6$ [24]. In $TmMn_1Fe_5Sn_6$ and $TmFe_6Sn_6$, M magnetic moments are aligned along the c axis, while this occurs at very low temperatures for $x = 4.25$ and 4.5 (Fig. 5).

Here, ^{119}Sn Mössbauer spectra of the two stannides with $x = 4.25$, 4.5, recorded at three different temperatures, are shown in Fig. 8. Two spectra recorded at 4.2 and 300 K are

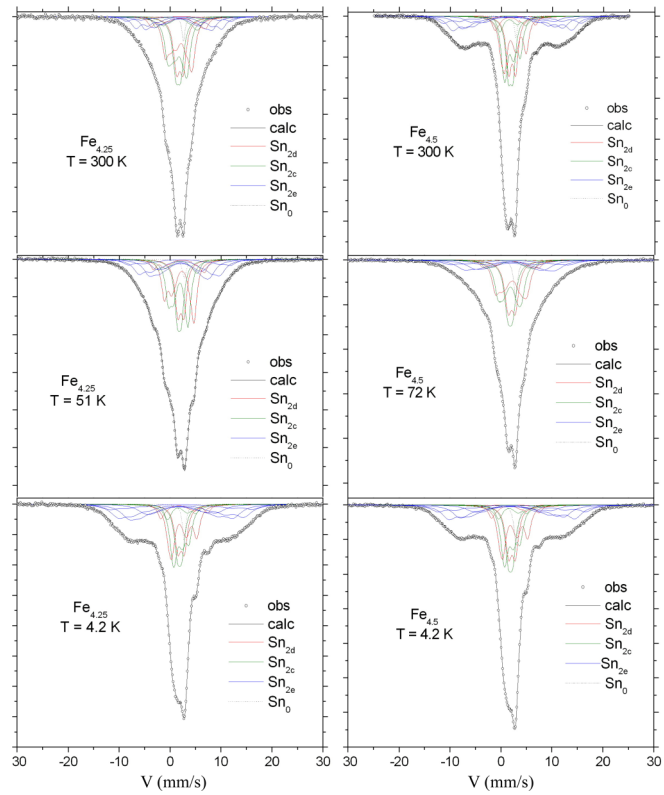

FIG. 8. Observed and calculated ^{119}Sn Mössbauer spectra of $TmMn_{6-x}Fe_xSn_6$ compounds (x = 4.25 and 4.5) with AFI antiferromagnetic structures at various temperatures.

shown in Fig. S7 for $x = 5$ and in Fig. S8 for $x = 6$ (Sec. X B in the Supplemental Material [1]).

Because of the AFI structure, spectra consist mainly of an intense and broad central component clearly constituted of various subspectra with small hyperfine magnetic fields, due to Sn(2c) and Sn(2d) sites and of broad outer wings (Sec. IV B in the Supplemental Material [1]) with larger hyperfine magnetic fields associated with Sn(2e) sites. Tm atoms, which are not magnetically ordered >1.6 K (Sec. V B), do not contribute to the measured hyperfine magnetic fields.

Only Sn(2e) atoms have six magnetic neighbors ferromagnetically coupled in a single kagome plane. For $x = 6$, all tin sites have 6 Fe nearest neighbors, AFM coupled for Sn(2c) and Sn(2d) sites, with $N_{\mathrm{Fe}} = 0$, which give rise to the two central doublets of Fig. S9 in the Supplemental Material [1]. The magnetic components of $TmFe_6Sn_6$ spectra are due to Sn(2e) sites whose first nearest neighbors are ferromagnetically coupled. Figure S10 in the Supplemental Material [1] shows in addition the hyperfine magnetic field distribution at the Sn(2e) sites calculated at 4.2 K. Its asymmetry is further discussed in Sec. X B in the Supplemental Material [1].

The overlaps of subspectra in the central parts of Mössbauer spectra recorded for $x = 4.25$ and 4.5 require us to constrain their relative areas during the whole fitting process (Sec. IV A in the Supplemental Material [1]). Here, Sn(2c) and Sn(2d) peaks form a broad central component from which it is difficult to extract usable values of their hyperfine magnetic fields, as $B_{\mathrm{exp}}^{(2c)}$ and $B_{\mathrm{exp}}^{(2d)}$ are only ∼4–5 T.

The three tin sites are further considered in Secs. IX B and X in the Supplemental Material [1]. We limit the following discussion to Sn(2e) sites, whose hyperfine magnetic fields are large and quadrupole splittings are small (Sec. IV B in the Supplemental Material [1]). Reliable values of model parameters can then be derived from experimental results.

An overall decrease of the Sn(2e) hyperfine magnetic fields in $TmMn_{6-x}Fe_xSn_6$ ($x = 4.25$, 4.5), clearly seen without fitting, on the wings of the spectra of Fig. 8, takes place when T increases from 4.2 to 51 K ($x = 4.25$) or to 72 K ($x = 4.5$). This decrease is due primarily to the increase of the angle θ from ≈7.5(6)°, respectively, to ≈69° and ≈53° (Fig. 5), as further discussed in detail in Sec. IX B in the Supplemental Material [1].

1. Model parameters obtained from hyperfine magnetic fields measured at 4.2 K

The linear equations, which express $B_M^{(2e)}(p)$, are obtained from Eqs. (5) and (8):

$$B_M^{(2e)}(p) = B_M^{(2e)}(0) + p[A_{\mathrm{Fe}}(2e)\mu_{\mathrm{Fe}} - A_{\mathrm{Mn}}(2e)\mu_{\mathrm{Mn}}], \quad (12)$$

where $A_M(2e) = A_{isM}(2e) - A_{aeff,M}(2e)/3$ ($\theta = 0°$) and $B_M^{(2e)}(0) = 6A_{\mathrm{Mn}}(2e)\mu_{\mathrm{Mn}}$. As shown below, $|A_{\mathrm{Mn}}(2e)|$ is an order of magnitude smaller than $|A_{\mathrm{Fe}}(2e)|$. Therefore, the sign of $A_{\mathrm{Mn}}(2e)$ does not matter, all the more that observable subspectra come from Sn atoms with >3 Fe neighbors ($p \geqslant 3$, Table S6 in the Supplemental Material [1]). The hyperfine magnetic fields predicted from Eq. (12) are then written as

$$B_{\mathrm{pred}}^{(2e)}(p) = 6\varepsilon A_{\mathrm{Mn}}(2e)\mu_{\mathrm{Mn}} + p[|A_{\mathrm{Fe}}(2e)|\mu_{\mathrm{Fe}} - \varepsilon A_{\mathrm{Mn}}(2e)\mu_{\mathrm{Mn}}], \quad (13)$$

where $\varepsilon = \mathrm{sign}[A_{\mathrm{Fe}}(2e)]$. The experimental hyperfine magnetic fields vary linearly with p, $B_{\mathrm{exp}}^{(2e)}(p) = B_{\mathrm{exp}}^{(2e)}(0) + p\Delta B_{\mathrm{exp}}^{(2e)}$, with positive slopes, both at 4.2 K, for $x = 4.25$, 4.5, and 5, and at moderate temperatures (51 and 72 K; Fig. 7 and Table I).

The hyperfine magnetic fields $B_{\mathrm{exp}}^{(2e)}(6)$ at 4.2 K for $x = 4.25$, 4.5, and 5 (20.4, 21.2, and 22 T, respectively) and the corresponding magnetic moments at 2 K (2.35, 2.40, and 2.42μ_{B}, Table S5 in the Supplemental Material [1]) yield the values of $|A_{\mathrm{Fe}}(2e)| = B_{\mathrm{exp}}^{(2e)}(6)/(6\mu_{\mathrm{Fe}})$ [Eq. (13)], whose mean is $|A_{\mathrm{Fe}}(2e)| = 1.51(5)\,\mathrm{T}/\mu_{\mathrm{B}}$.

Further, the mean hyperfine magnetic field at 4.2 K, 23.2 T, of $TmFe_6Sn_6$, as obtained from the hyperfine magnetic field distribution (Fig. S10 in the Supplemental Material [1]), yields $|A_{\mathrm{Fe}}(2e)| = 1.61(3)\,\mathrm{T}/\mu_{\mathrm{B}}$. From the slope $\Delta B_{\mathrm{exp}}^{(2e)} = 3.3$ T, we get thus $\varepsilon A_{\mathrm{Mn}}(2e) = 0.08(8)\,\mathrm{T}/\mu_{\mathrm{B}}$ [Eq. (13)], which is an order of magnitude smaller than $|A_{\mathrm{Fe}}(2e)|$. The $|A_{\mathrm{Fe}}(2e)|$ value at 4.2 K is shown below to be consistent with the value derived from moment rotation between 4.2 and ∼50–70 K.

2. Model parameters obtained from magnetic moment rotation with temperature

The variation of $B_{\mathrm{exp}}^{(2e)}(6)$ due to the temperature-dependent angle θ (Fig. 5) yields $\rho_{\mathrm{eff,Fe}}^{(2e)} = -0.80 \pm 0.06$ and -0.84 ± 0.14 for $x = 4.25$ and 4.5, respectively (Sec. IX in the Supplemental Material [1]). Negative ratios $\rho_{\mathrm{Fe}}^{(2e)} = A_{a,\mathrm{Fe}}(2e)/A_{is\mathrm{Fe}}(2e)$ contrast with positive ratios $A_{a,\mathrm{Mn}}(2h)/A_{is\mathrm{Mn}}(2h)$ (h = c, d, e) found for Mn-rich alloys [21], which implies that $A_{a,\mathrm{Mn}}(2h)$ is negative, as is $A_{is\mathrm{Mn}}(2h)$ [17]. Negative anisotropic and isotropic components of hyperfine magnetic fields are also found for ^{119}Sn in $TmFe_2$ [35]. The previous results suggest that the negative sign of $\rho_{\mathrm{Fe}}^{(2e)}$ means that $A_{is\mathrm{Fe}}(2e)$ is now positive, as is then $B_{\mathrm{exp}}^{(2e)}(p)$, a fact made reasonable from the band structure calculations mentioned in Sec. IX.

The previous discussion means that $\varepsilon = 1$ in Eq. (13) for Fe-rich stannides. Values $A_{is\mathrm{Fe}}(2e) = 1.15(3)\,\mathrm{T}/\mu_{\mathrm{B}}$ and $A_{a\mathrm{Fe}}(2e) = -1.18(10)\,\mathrm{T}/\mu_{\mathrm{B}}$ are finally calculated from $\rho_{\mathrm{eff,Fe}}^{(2e)}$ in Sec. IX in the Supplemental Material [1].

In summary,

(a) for Mn-rich stannides, $A_{\mathrm{Fe}}(2e) = -0.44(8)\,\mathrm{T}/\mu_{\mathrm{B}}$, $A_{\mathrm{Mn}}(2e) = -1.53(7)\,\mathrm{T}/\mu_{\mathrm{B}}$, and

(b) for Fe-rich stannides, $A_{\mathrm{Fe}}(2e) = 1.51(5)\,\mathrm{T}/\mu_{\mathrm{B}}$, $|A_{\mathrm{Mn}}(2e)| = 0.08(8)\,\mathrm{T}/\mu_{\mathrm{B}}$, $A_{is\mathrm{Fe}}(2e) = 1.15(3)\,\mathrm{T}/\mu_{\mathrm{B}}$, and $A_{a\mathrm{Fe}}(2e) = -1.18(10)\,\mathrm{T}/\mu_{\mathrm{B}}$.

The marked decrease of the magnitude of $|A_{\mathrm{Mn}}(2e)|$ when going from Mn- to Fe-rich stannides agrees with the discussion presented below. The magnitudes of Mn coefficients in Fe-rich stannides are too small to decide if they are negative or positive.

IX. DISCUSSION AND CONCLUSIONS

Magnetic structures of Mn-rich ($x = 0.4$, 0.6, 1.2) and Fe-rich ($x = 4.25$, 4.5, 5) $TmMn_{6-x}Fe_xSn_6$ stannides, with $HfFe_6Ge_6$-type structure, were determined by magnetization measurements and neutron diffraction. The low-temperature magnetic properties of Mn-rich stannides (<∼20 K) are

complex and originate from a mixture of several magnetic phases, some being incommensurate. Our magnetic studies show that Tm atoms are not magnetically ordered at temperatures $>\sim$20 to 50 K in Mn-rich stannides ($x = 0.4, 0.6, 1.2$) and >1.6 K in Fe-rich stannides. In these temperature ranges, Mn- and Fe-rich stannides have different AFM structures, AFII and AFI, respectively. In both cases, Mn and Fe atoms of any kagome plane are ferromagnetically coupled. Structure AFII is such that two successive kagome planes are either ferromagnetically or AFM coupled, while they are AFM coupled for structure AFI.

The focus of the study of ^{119}Sn hyperfine magnetic fields was put on stannides, which have either an AFII or an AFI magnetic structure. The hyperfine magnetic fields are modeled as sums of anisotropic dipolar contributions and isotropic contributions. Both are due to magnetic moments of the six first nearest neighbors (Mn or Fe) of any tin site. The model includes isotropic and anisotropic constants, four in number, associated respectively with Sn-Mn and Sn-Fe bonds. With the assumption of a random substitution of Mn with Fe, the model predicts linear dependencies of average hyperfine magnetic fields:

(a) Sn(2d) atoms in Mn-rich stannides (AFII) and Sn(2e) atoms in all stannides have six ferromagnetically coupled neighbors, respectively, in two successive kagome planes and a single kagome plane. Their average hyperfine magnetic fields vary linearly with the number p of their first Fe nearest neighbors ($0 \leqslant p \leqslant 6$).

(b) If a given Sn atom is sandwiched between two AFM coupled kagome planes, then its associated average hyperfine magnetic field is predicted proportional to $N_{\mathrm{Fe}} = |p_2 - p_1|$, where one of the two kagome planes contains p_1 nearest neighbor Fe atoms and the other p_2. This is the case of Sn(2c) atoms in Mn-rich stannides (AFII) and Sn(2c) and Sn(2d) atoms in Fe-rich stannides (AFI).

Significant experimental results from ^{119}Sn Mössbauer spectra, associated with the largest hyperfine magnetic fields [Sn(2d) in Mn-rich stannides and Sn(2e) in all cases], agree with these predictions. Importantly, the slope of the line of experimental Sn(2e) hyperfine magnetic fields vs p is negative in Mn-rich stannides and positive in Fe-rich stannides. Experimental information enables us to determine only two linear combinations of the four constants mentioned above. In Fe-rich stannides, consistent values of the latter combinations are deduced, on the one hand, from the experimental Sn(2e) hyperfine magnetic fields vs p at 4.2 K and, on the other hand, from the variations of the largest hyperfine magnetic fields due to a temperature-dependent rotation of Mn and of Fe magnetic moments.

Our experimental results for Mn-rich stannides agree with published results which show that the isotropic constants of Sn-Mn bonds are all negative. Further, the ratios of Sn-Mn anisotropic constants to their associated isotropic constants are positive. Therefore, the anisotropic constants are negative too.

In Fe-rich stannides, the temperature-dependent rotation of Mn and of Fe magnetic moments enables us to calculate separately the anisotropic and isotropic constants of Sn(2e)-Fe bonds whose ratio is concluded to be negative. A change of sign of the isotropic constant of Sn(2e)-Fe bonds explains a change of sign of the resulting average hyperfine magnetic fields and the slope of their variation with p.

A rigid band approach was used to account for a change from large negative tin hyperfine magnetic fields in $R\mathrm{Mn_6Sn_6}$ to positive germanium hyperfine magnetic fields in $R\mathrm{Fe_6Ge_6}$ [36]. Only the bonding s-d hybrids are occupied in Mn-based stannides, while the supplementary valence electrons brought by Fe partly populate the antibonding states in Fe-based germanides [36]. This evolution leads to a change of hyperfine magnetic field signs. An evolution from negative Sn(2e) hyperfine magnetic fields in Mn-rich stannides to positive Sn(2e) hyperfine magnetic fields in Fe-rich stannides is in line with the previous explanation. The range of Fe content in which this change of sign occurs remains to be investigated. In a similar way, we observe that the magnitudes of the constants associated with Sn(2e)-Mn bonds decrease strongly when going from Mn- to Fe-rich stannides.

ACKNOWLEDGMENTS

We are indebted to the Institut Laue-Langevin (Grenoble, France) for the provision of research facilities (Exp. n_5-31-1854) and to Dr. B. Ouladdiaf for his help during the measurements.

[1] See Supplemental Material at http://link.aps.org/supplemental/10.1103/PhysRevB.104.184433 for further information on crystallographic characteristics of $\mathrm{TmMn_{6-x}Fe_xSn_6}$ stannides, on magnetization and neutron diffraction results, on fitting assumptions of ^{119}Sn Mössbauer spectra, on models of ^{119}Sn transferred hyperfine magnetic fields in Mn- and Fe-rich stannides, and on their contribution to the analysis of experimental results.

[2] N. J. Ghimire and I. I. Mazin, Nat. Mater. **19**, 137 (2020).

[3] N. J. Ghimire, R. L. Dally, L. Poudel, D. C. Jones, D. Michel, N. Thapa Magar, M. Bleuel, M. A. McGuire, J. S. Jiang, J. F. Mitchell, J. W. Lynn, and I. I. Mazin, Sci. Adv. **6**, 51 (2020).

[4] R. L. Dally, J. W. Lynn, N. J. Ghimire, D. Michel, P. Siegfried, and I. I. Mazin, Phys. Rev. B **103**, 094413 (2021).

[5] M. Li, Q. Wang, G. Wang, Z. Yuan, W. Song, R. Lou, Z. Liu, Y. Huang, Z. Liu, H. Lei, Z. Yin, and S. Wang, Nat. Commun. **12**, 3129 (2021).

[6] Q. Wang, K. J. Neubauer, C. Duan, Q. Yin, S. Fujitsu, H. Hosono, F. Ye, R. Zhang, S. Chi, K. Krycka, H. Lei, and P. Dai, Phys. Rev. B **103**, 014416 (2021).

[7] C. Q. Xu, T. W. Heitmann, H. Zhang, X. Xu, and X. Ke, Phys. Rev. B **104**, 024413 (2021).

[8] J.-X. Yin, W. Ma, T. A. Cochran, X. Xu, S. S. Zhang, H.-J. Tien, N. Shumiya, G. Cheng, K. Jiang, B. Lian *et al.*, Nature (London) **583**, 533 (2020).

[9] W. Ma, X. Xu, J.-X. Yin, H. Yang, H. Zhou, Z.-J. Cheng, Y. Huang, Z. Qu, F. Wang, M. Zahid Hasan, and S. Jia, Phys. Rev. Lett. **126**, 246602 (2021).
[10] Z. Liu, N. Zhao, M. Li, Q. Yin, Q. Wang, Z. Liu, D. Shen, Y. Huang, H. Lei, K. Liu, and S. Wang, Phys. Rev. B **104**, 115122 (2021).
[11] W. Ma, X. Xu, Z. Wang, H. Zhou, M. Marshall, Z. Qu, W. Xie, and S. Jia, Phys. Rev. B **103**, 235109 (2021).
[12] D. Chen, C. Le, C. Fu, H. Lin, W. Schnelle, Y. Sun, and C. Felser, Phys. Rev. B **103**, 144410 (2021).
[13] T. Mazet, H. Ihou-Moko, J. F. Marêché, and B. Malaman, Eur. Phys. J. B **51**, 173 (2006).
[14] F. Weitzer, A. Leithejasper, K. Hiebl, P. Rogl, Q. N. Qi, and J. M. D. Coey, J. Appl. Phys. **73**, 8447 (1993).
[15] Y. Amako, T. Yamamoto, and H. Nagai, Hyperfine Interact. **94**, 1897 (1994).
[16] J. M. Cadogan, Suharyana, D. H. Ryan, O. Moze, and W. Kockelmann, J. Appl. Phys. **87**, 6046 (2000).
[17] T. Mazet, J. Tobola, G. Venturini, and B. Malaman, Phys. Rev. B **65**, 104406 (2002).
[18] F. Grandjean, G. J. Long, B. Mahieu, J. Han, and W. J. James, J. Phys.: Condens. Matter **17**, 4665 (2005).
[19] P. Gaszyński, L. C. J. Pereira, and J. C. Waerenborgh, J. Alloys Compd. **451**, 484 (2008).
[20] G. Venturini and B. Malaman, J. Magn. Magn. Mater. **377**, 159 (2015).
[21] L. K. Perry, D. H. Ryan, and G. Venturini, Phys. Rev. B **75**, 144417 (2007).
[22] L. K. Perry, D. H. Ryan, G. Venturini, and J. M. Cadogan, J. Appl. Phys. **99**, 08J302 (2006).
[23] L. K. Perry, D. H. Ryan, and G. Venturini, Hyperfine Interact. **170**, 105 (2006).
[24] J. Bourgeois, G. Venturini, and B. Malaman, J. Alloys Compd. **480**, 171 (2009).
[25] T. Mazet and B. Malaman, J. Magn. Magn. Mater. **219**, 33 (2000).
[26] G. Venturini, P. Lemoine, and B. Malaman, J. Magn. Magn. Mater. **354**, 21 (2014).
[27] J. Rodriguez-Carvajal, Physica B **192**, 55 (1993).
[28] G. Le Caër and J. M. Dubois, J. Phys. E: Sci. Instrum. **12**, 1083 (1979).
[29] G. Le Caër, B. Malaman, G. Venturini, and I. B. Kim, Phys. Rev. B **26**, 5085 (1982).
[30] L. M. Corliss and J. M. Hastings, J. Appl. Phys. **39**, 461 (1968).
[31] G. Venturini, B. Malaman, G. Le Caër, and D. Fruchart, Phys. Rev. B **35**, 7038 (1987).
[32] G. Le Caër, B. Malaman, G. Venturini, D. Fruchart, and B. Roques, J. Phys. F: Met. Phys. **15**, 1813 (1985).
[33] G. Le Caër, B. Malaman, G. Venturini, H. G. Wagner, and U. Gonser, Hyperfine Interact. **28**, 631 (1986).
[34] V. I. Krylov, B. Bosch-Santos, G. A. Cabrera-Pasca, N. N. Delyagin, and A. W. Carbonari, AIP Advances **6**, 056024 (2016).
[35] N. N. Delyagin, G. T. Mudzhiri, V. I. Nesterov, and A. K. Churakov, Zh. Eksp. Teor. Fiz. **89**, 2149 (1985) [Sov. Phys. JETP **62**, 1240 (1986)].
[36] T. Mazet, J. Tobola, and B. Malaman, Eur. Phys. J. B **33**, 183 (2003).